The Astrophysical Journal, 981:164 (7pp), 2025 March 10 https://doi.org/10.3847/1538-4357/adb1e2

Can the Dynamo of Spiral-arm Galaxies Be Explained by Anisotropic Conductivity?

Paul Gomez[1], Franck Plunian[2], and Thierry Alboussière[1]
[1] Université Lyon 1, ENS de Lyon, CNRS, Laboratoire de Géologie de Lyon, Lyon 69622, France; paul.gomez@univ-lyon1.fr, thierry.alboussiere@ens-lyon.fr
[2] Université Grenoble Alpes, University of Savoie Mont Blanc, CNRS, IRD, Université Gustave Eiffel, ISTerre, 38000 Grenoble, France; franck.plunian@univ-grenoble-alpes.fr
Received 2024 September 10; revised 2025 January 22; accepted 2025 February 2; published 2025 March 6

Abstract

The possibility of generating a magnetic field by a dynamo effect with anisotropic electrical conductivity rather than turbulent flow has been demonstrated theoretically and experimentally. If the electrical conductivity is anisotropic, the electrical currents will flow preferentially in certain directions rather than others, and a simple differential rotation will suffice to generate a magnetic field. In a galaxy with spiral arms, it is reasonable to assume that the electrical conductivity will be twice as large along the arms than in the perpendicular direction, suggesting the possibility of an anisotropic dynamo. However, a further geometrical criterion must be satisfied to obtain a dynamo. It is given by $\Omega' \cdot \sin p > 0$, where p is the pitch angle of the spiral arms, with $p \in [-\frac{\pi}{2}, \frac{\pi}{2}]$, and Ω' is the radial shear of the angular velocity. We find that the usual spiral-arm galaxies, which satisfy $|\Omega'| < 0$, do not satisfy this dynamo condition because they have trailing arms instead of leading arms. Even galaxy NGC 4622, which has both trailing and leading arms, does not satisfy this dynamo condition either. This is confirmed by numerical simulations of the induction equation. Thus, for all spiral-arm galaxies known to date, the anisotropy of the spiral arms cannot explain the existence of galactic magnetic fields until further notice.

Unified Astronomy Thesaurus concepts: Galaxy magnetic fields (604)

1. Introduction

Galactic magnetic fields have been observed for decades, raising questions about their role in the formation and behavior of galaxies. They are composed of a large-scale coherent part and a small-scale random part due to turbulence. A typical timescale for turbulent magnetic diffusion in galaxies is 10^8 yr. This corresponds to about one tenth of the age of a galaxy, implying that a physical mechanism is needed to explain why galactic magnetic fields are still present. Assuming that a galaxy can be modeled by a rotating plasma, the dynamo effect is a good candidate to explain the generation of galactic magnetic fields (A. Brandenburg & K. Subramanian 2005; R. Beck et al. 2019). Since the pioneering work of F. Krause & K.-H. Rädler (1980), an alpha effect due to small-scale helical turbulence, conjugated to a strong differential rotation, has been proposed as the main dynamo mechanism.

The magnetic Reynolds number is defined by

$$R_m = \sigma \mu U L, \tag{1}$$

where σ is the electrical conductivity of a fluid, μ is its magnetic permeability, and U and L are two characteristic values of velocity and length scale. This dimensionless number can be understood as the ratio of the magnetic diffusion time by the flow turnover time, implying that a necessary condition for dynamo action is $R_m > 1$. In galaxies, $R_m \approx 10^{18}$–10^{20} (A. A. Schekochihin et al. 2002; A. Brandenburg & K. Subramanian 2005), much higher than that required for dynamo action. However, a question arises: is the dynamo still efficient at high R_m or, in other words, is the dynamo of a fast type (S. Childress & A. D. Gilbert 2008)? A fast dynamo corresponds to a strictly positive kinematic growth rate of the magnetic field, as opposed to a slow dynamo for which the magnetic growth rate vanishes in the limit of a high R_m. The turbulent alpha effect is suspected to quench at high R_m due to nonlinear effects, challenging the usual dynamo mechanism advocated to explain the galactic magnetic field. (F. Rincon 2019).

Another possibility for generating a magnetic field by a dynamo effect has recently been proposed (T. Alboussière et al. 2020; F. Plunian & T. Alboussière 2020). It is based on large-scale differential rotation and anisotropic electrical conductivity. Turbulence is not necessary for this dynamo mechanism to work. Assuming complete axisymmetry, it has been shown that an anisotropic dynamo can occur provided the differential rotation is higher than a certain threshold, depending on the properties of the anisotropy (F. Plunian & T. Alboussière 2020). For an angular velocity with a smooth radial profile, an asymptotic approach has shown that the anisotropic dynamo is fast (F. Plunian & T. Alboussière 2022), then proving to be an interesting candidate for a galactic dynamo. Anisotropic dynamo action has also been demonstrated experimentally (T. Alboussière et al. 2022). Although the geometry of this experiment is different from that of a galaxy, they both share a logarithmic spiral anisotropy of electrical conductivity.

In this paper, we study the possibility of a spiral-arm galaxy working as an anisotropic dynamo. In Section 2, the modeling of the anisotropic dynamo is explained. In Section 3, the results of some simulations are shown, for several rotation profiles and several arms configurations—trailing, leading arms, or a combination of both.

2. Modeling

2.1. The Pitch Angle p

The shape of galactic spiral arms can be approximated by logarithmic spirals (M. Seigar & P. James 1998) with a constant pitch angle p, although in reality this can vary by a

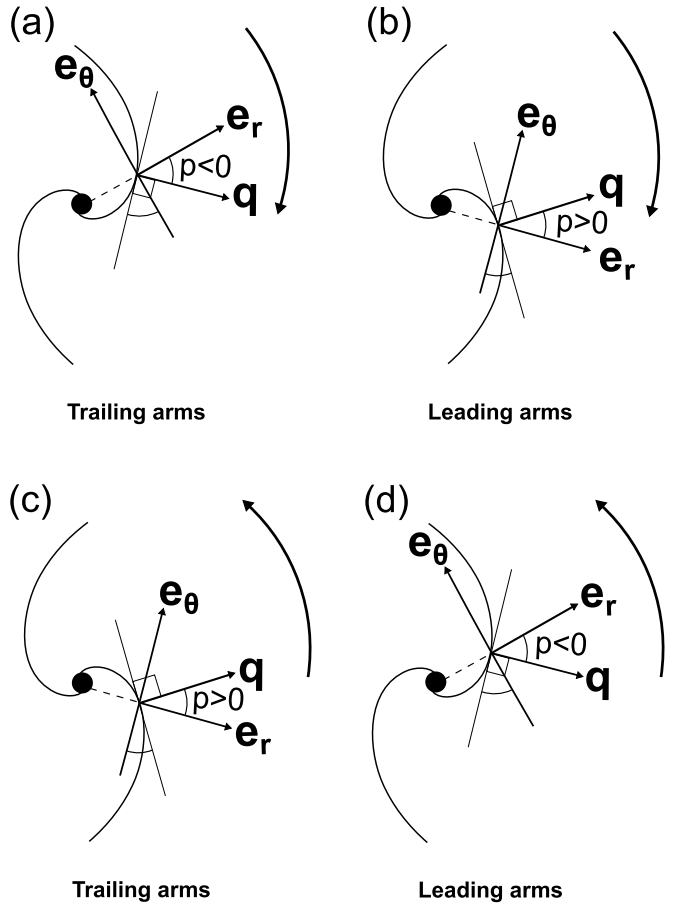

Figure 1. Examples of leading and trailing arms, with positive or negative pitch angles p. In (a) and (b), the galaxy rotates clockwise. In (d) and (c), the galaxy rotates counterclockwise.

few degrees (S. Savchenko & V. Reshetnikov 2013). Following B. L. Davis et al. (2012), the absolute value of p is defined as the smallest angle between the azimuthal direction and the tangential direction of the spiral, at a given radius. In addition, the sign of p defines the chirality of the spiral. A clockwise outward or counterclockwise inward winding corresponds to $p > 0$, and a clockwise inward or counterclockwise outward winding corresponds to $p < 0$, as illustrated in Figure 1.

Denoted by $\boldsymbol{q}$, the unit vector normal to the spiral is defined by

$$\boldsymbol{q} = \cos p\ \boldsymbol{e}_r + \sin p\ \boldsymbol{e}_\theta, \tag{2}$$

with $p \in [-\frac{\pi}{2}, \frac{\pi}{2}]$, and where $(\boldsymbol{e}_r, \boldsymbol{e}_\theta, \boldsymbol{e}_z)$ is the cylindrical coordinate system. Depending on the chirality and the pitch angle, the galaxy's arms are either trailing arms or leading arms, as illustrated in Figure 1. A leading arm has its outer tip pointing in the direction of the galaxy's rotation, whereas the outer tip of a trailing arm points in the opposite direction of rotation.

2.2. Anisotropic Electrical Conductivity

In galaxies, the electron density is greater in the spiral arms than in the interarm regions by a factor of 2 (L. Gutiérrez & J. E. Beckman 2010). However, the Spitzer resistivity does not depend on the electron density (L. Spitzer & R. Härm 1953) and then cannot lead to anisotropic electrical conductivity. A candidate for such anisotropy can be the different abundance of H II regions within the spiral arm and interarm regions (J. Knapen 1998). Another option could be to rely on the turbulent diffusivity, which is most effective in the spiral arms.

We define anisotropic effective electrical conductivity as a tensor (M. Ruderman & A. Ruzmaikin 1984),

$$[\sigma_{ij}] = \sigma_\perp \delta_{ij} + (\sigma_\parallel - \sigma_\perp) q_i q_j, \tag{3}$$

where $\sigma_\parallel$ and $\sigma_\perp$ are the electric conductivity in the directions parallel and perpendicular to $\boldsymbol{q}$. We do not have an estimate for the ratio $\sigma_\perp/\sigma_\parallel$, but the key point is that it must be strictly larger than unity. For the numerical applications, we choose $\sigma_\perp/\sigma_\parallel = 2$.

We note that the conductivity model given by (3) implies that the conductivity is axisymmetric, which is obviously not the case, since the spiral arms break this axisymmetry. It is, however, the simplest and probably the most dynamo-capable model we can think of for studying the possibility of an anisotropic dynamo in galaxies.

2.3. Induction Equation

The induction equation can be written as

$$\partial_t \boldsymbol{B} = \nabla \times (\boldsymbol{U} \times \boldsymbol{B}) - \mu_0^{-1} \nabla \times ([\sigma_{ij}]^{-1} \nabla \times \boldsymbol{B}), \tag{4}$$

where $\boldsymbol{B}(r, t)$ is the magnetic induction, $\boldsymbol{U} = U(r)\boldsymbol{e}_\theta$, and μ_0 is the vacuum magnetic permeability.

Since the velocity is stationary, and assuming axisymmetry, we look for a magnetic induction in the form

$$\boldsymbol{B} = \boldsymbol{B}(r, z)\exp(\gamma t), \tag{5}$$

leading to the resolution of a 2D eigenvalue problem. In (5), $\gamma > 0$ is the signature of dynamo action, the dynamo threshold corresponding to $\gamma = 0$.

2.4. A Necessary Condition for Dynamo Action

In F. Plunian & T. Alboussière (2022), an asymptotic expression of the magnetic growth rate γ for $R_m \gg 1$ and $\sigma_\perp \gg \sigma_\parallel$ has been derived:

$$\gamma \approx r_0 \cdot \Omega'(r_0) \cdot \cos p \cdot \sin p - K^2, \tag{6}$$

where $\Omega'(r)$ is the radial derivative of the angular velocity $\Omega(r) = U(r)/r$, K is a dimensionless number, and r_0 is a value of r at which the asymptotic expansion leading to (6) has been made.

For $p \in [-\frac{\pi}{2}, \frac{\pi}{2}]$, a necessary condition for anisotropic dynamo action is therefore that there must be at least one value of r such that

$$\Omega' \cdot \sin p > 0. \tag{7}$$

Then, applying (7) to cases (a)–(d), and depending on whether the absolute value of the angular velocity $|\Omega|$ is decreasing ($|\Omega|' < 0$) or increasing ($|\Omega|' > 0$), the sign of $\Omega' \cdot \sin p$ can be determined (see Table 1). We find that, if $|\Omega(r)|$ decreases (increases), the dynamo is only possible in cases (b) and (d) (or cases (a) and (c), respectively).

Table 1
Sign of $\Omega' \cdot \sin p$ for Cases (a)–(d) Depicted in Figure 1

	Ω	p	$\lvert\Omega\rvert'$	Ω'	$\Omega' \cdot \sin p$
Trailing (a)	−	−	+	−	+
			−	+	−
Leading (b)	−	+	+	−	−
			−	+	+
Trailing (c)	+	+	+	+	+
			−	−	−
Leading (d)	+	−	+	+	−
			−	−	+

2.5. Application to Usual Spiral-arm Galaxies

The central part of a galaxy, called the bulge, is made of a high concentration of stars. In the vast majority of spiral-arm galaxies observed so far, the azimuthal velocity $U(r)$ is a solid body rotation within the bulge, and is flat outside the bulge (V. C. Rubin et al. 1982; Y. Sofue & V. Rubin 2001). This corresponds to an angular velocity $\Omega(r)$ that is constant within the bulge and whose absolute value decreases outside, corresponding to $|\Omega|' \leqslant 0$. From Table 1, only cases (b) and (d) are likely to behave as anisotropic dynamos. They both correspond to a leading arms geometry (Figure 1). However, all galaxies observed so far have trailing arms (I. Pasha & M. Smirnov 1982), so they are unlikely to be the seat of an anisotropic dynamo.

2.6. NGC 4622: An Unusual Spiral-arm Galaxy

The spiral-arm galaxy NGC 4622 possesses one trailing arm surrounded by two leading arms (G. Byrd & S. Howard 2019), as illustrated in Figure 2(a). The trailing arm corresponds to case (a), and the two leading arms to case (b). In addition, according to Figure 2(b), the azimuthal velocity is flat for the trailing arm ($|\Omega|' < 0$) and increasing in absolute value for the leading arms ($|\Omega|' > 0$), leading in both cases to $\Omega' \cdot \sin p < 0$. Once again, it is therefore unlikely that galaxy NGC 4622 is the seat of an anisotropic dynamo.

3. Numerical Simulations

In order to verify the theoretical conclusions of Sections 2.5 and 2.6, we now carry out numerical simulations.

3.1. Velocity Profiles

The geometry of a spiral-arm galaxy is approximated by a cylinder of height h and radius $R \gg h$. The radius of the galactic bulge is denoted r_b. Most spiral-arm galaxies have dimensions $r_b \sim h \approx 0.2$–2 kpc and $R \approx$ 10–50 kpc (M. Mollá et al. 2000; C. Möllenhoff 2004; Y.-H. Zhao et al. 2004). In the simulations, we take $r_b = h$ and $R/r_b = 50$. For the NGC 4622 galaxy, according to R. J. Buta et al. (2003), $r_b \approx 8''.8$, $R \approx 52''$, and $h \sim 1''.93$ ($5\,\mathrm{kpc} = 29''.7$). In the simulations, we take $R/h = 27$ and $r_b/h = 4.6$.

We consider four azimuthal velocity profiles, U_K, U_F, U_S, and U_{4622}. The first two, U_K and U_F, correspond to a velocity profile that is a solid body rotation within the bulge and, respectively, Keplerian or flat outside the bulge. The last two, U_S and U_{4622}, are smooth functions of r close to solid rotation for $r \ll r_b$, and (i) asymptotically flat in the limit $r \gg 1$ for U_S and (ii) corresponding to the observations of NGC 4622 given by the red triangles in Figure 2(b) for U_{4622}.

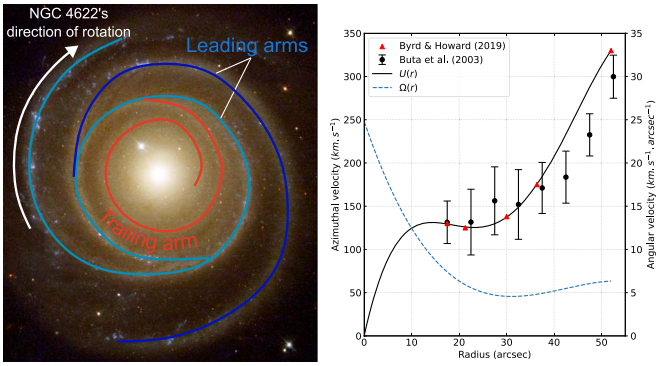

(a) (b)

Figure 2. (a) Illustration of the trailing and leading arms of the NGC 4622 galaxy. (b) The black dots and red triangles correspond to observations of the azimuthal velocity $U(r)$ by R. J. Buta et al. (2003) and G. Byrd & S. Howard (2019), respectively. The full curve is a fit of the red triangles, corresponding to $U(r)$, and the dashed curve to $\Omega(r) = U(r)/r$.

They are given by

$$U_K(r) = \begin{cases} U_0 r/r_b & \text{for} \quad 0 \leqslant r \leqslant r_b \\ U_0\sqrt{r_b/r} & \text{for} \quad r_b \leqslant r \leqslant R \end{cases}, \tag{8}$$

$$U_F(r) = \begin{cases} U_0 r/r_b & \text{for} \quad 0 \leqslant r \leqslant r_b \\ U_0 & \text{for} \quad r_b \leqslant r \leqslant R \end{cases}, \tag{9}$$

$$U_S(r) = U_0 \tanh\left(\frac{ar}{r_b}\right) \text{for } 0 \leqslant r \leqslant R, \tag{10}$$

$$U_{4622}(r) = U_0(br + cr^2 + dr^3 + er^4) \text{for } 0 \leqslant r \leqslant R. \tag{11}$$

In (10), we set $U_S(r_b) = U_0$, implying that $a = 3.8$. The parameters r_b and U_0 are the characteristic scale and velocity by which the induction Equation (4) is normalized; the problem then depends only on the magnetic Reynolds number:

$$R_m = \sigma_\perp \mu_0 U_0 r_b, \tag{12}$$

where μ_0 is the magnetic permeability of the void. As an example, shown in Figure 3(a), taking $U_0 = 233$ km s^{-1} and $r_b = 1$ kpc in (3.1) and (10) leads to a reasonable approximation of the velocity profile measured in NGC 7331 (K. Begeman 1987). The corresponding angular velocity $\Omega(r) = U(r)/r$ is given in Figure 3(b). Although not represented, the value of Ω_S at $r = 0$ is equal to $885.4\,\mathrm{km\,s^{-1}\,kpc^{-1}}$.

In (11), the coefficients b, c, d, and e are derived from a fourth-order polynomial regression in order to fit the data by G. Byrd & S. Howard (2019) given by the red triangles in Figure 2(b). They are given by $b = 7.523 \times 10^{-2}\,\mathrm{arcsec^{-1}}$, $c = -4.896 \times 10^{-3}\,\mathrm{arcsec^{-2}}$, $d = 1.244 \times 10^{-4}\,\mathrm{arcsec^{-3}}$, and $e = -9.805 \times 10^{-7}\,\mathrm{arcsec^{-4}}$. In Figure 2(b), the full curve corresponds to $U(r)$ given by (11) with $U_0 = 330\,\mathrm{km\,s^{-1}}$, and the dashed curve to $\Omega(r) = U(r)/r$. We note that $\Omega' = 0$ for $r \approx 30''$ (G. Byrd & S. Howard 2019).

3.2. Values Taken for the Pitch Angle

According to R. Buta et al. (1992), in galaxy NGC 4622, the pitch angle is $p = -3^\circ.8$ for the part corresponding to the trailing arm (and $p = 7^\circ.5$ for the leading arms). For other spiral-arm

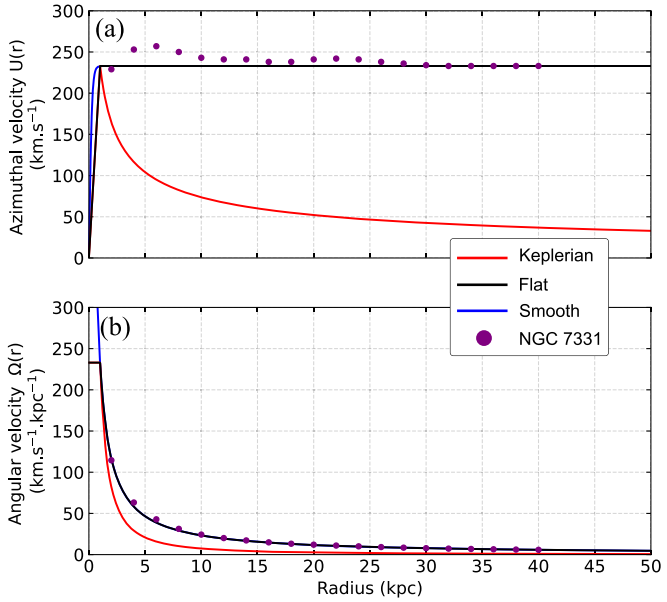

Figure 3. (a) Azimuthal velocity $U(r)$. (b) Angular velocity $\Omega(r) = U(r)/r$. They are given for the three profiles Keplerian (K), flat (F), and smooth (S), and from observations of galaxy NGC 7331 (K. Begeman 1987). For $r \geqslant 1$, the flat and smooth curves coincide.

galaxies, the pitch angle varies between 10° and 50° (M. S. Seigar et al. 2006), and we take the mean value $p = 28°$.

3.3. Poloidal–Toroidal Decomposition

The simulations are performed using Freefem++, a partial differential equation solver that employs the finite element method (F. Hecht 2012). We use a poloidal–toroidal decomposition of $\boldsymbol{B}$,

$$\boldsymbol{B} = \nabla \times (P(r, z)\boldsymbol{e}_\theta) + T(r, z)\boldsymbol{e}_\theta, \tag{13}$$

such that the solenoidality condition $\nabla \cdot \boldsymbol{B} = 0$ is necessarily satisfied.

The problem is axisymmetric. In the (r, z)-plane, the galaxy is modeled by a rectangle of dimensions $h \times R$, and the computational domain is a semidisk of radius R' (see Figure 4(a)). The electrical conductivity tensor is defined by (3) in the rectangle, and zero elsewhere. The corresponding boundary conditions are

$$T(r = 0) = P(r = 0) = T\left(z = \pm\frac{h}{2}, r \leqslant R\right) = 0, \tag{14}$$

the last condition insuring that, at the border of the conducting domain, the normal component of the current density vanishes. For $\rho = R'$ with $\rho = \sqrt{r^2 + z^2}$, we impose

$$T(\rho = R') = \left(\frac{\partial P}{\partial r} - \frac{P}{R'}\right)(r = R') = 0, \tag{15}$$

meaning that the magnetic field matches with a dipolar magnetic field at the limit of the computational domain $\rho = R'$.

3.4. Growth Rates

In Figure 5, the magnetic growth rate γ is plotted versus R_m for each velocity profile (8–11). As predicted in Sections 2.5 and 2.6, a dynamo ($\gamma > 0$) is only possible if we replace U_S,

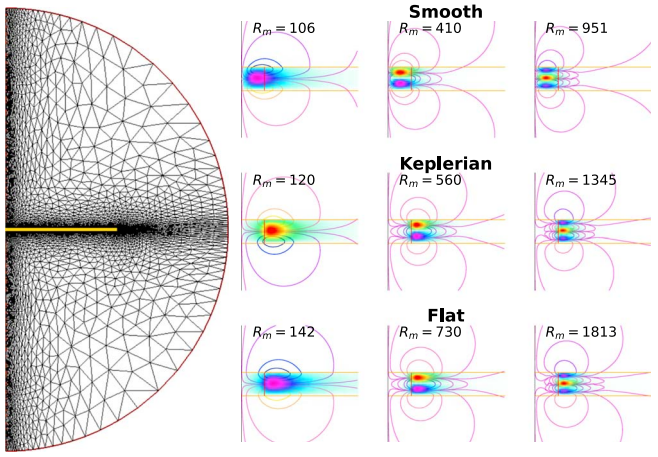

Figure 4. Left: meshing domain for numerical simulations. Right: isovalues of the poloidal and toroidal components of the magnetic field for smooth, Keplerian, and flat azimuthal velocity profiles at different R_m. The axis of rotation is represented by the vertical black line. The radial limit of the bulge is represented by the vertical red line. The conducting domain lies between the two horizontal orange lines. Increasing R_m, we see that the magnetic mode evolves from quadrupolar (left), to octopolar (middle), and to a higher mode (right).

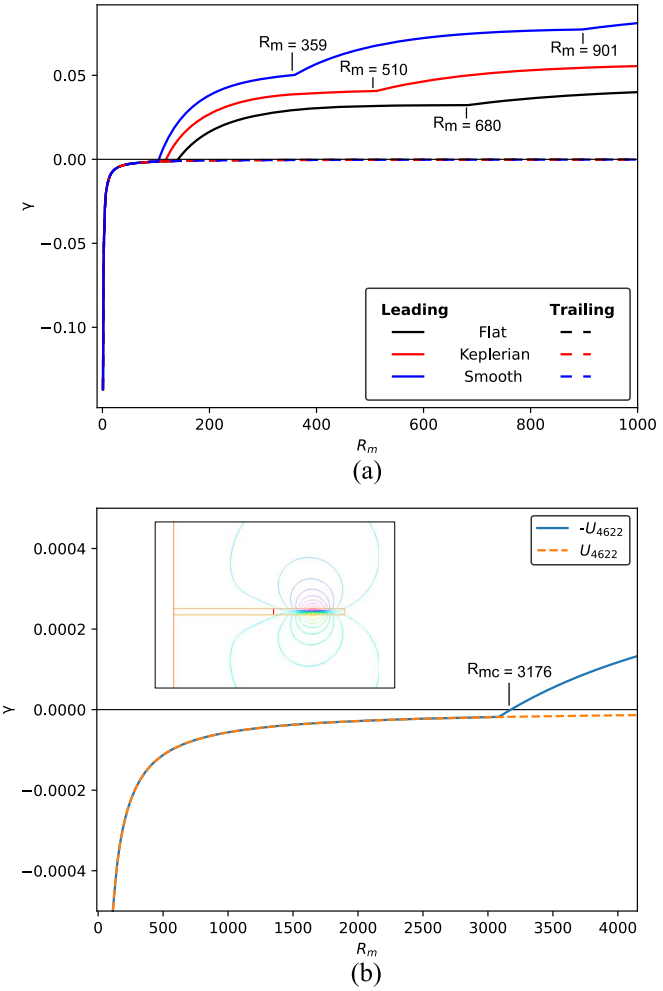

Figure 5. (a) Growth rate γ vs. R_m for U_K, U_F, and U_S (dashed curves) and $-U_K$, $-U_F$, and $-U_S$ (solid curves). (b) Growth rate γ vs. R_m for U_{4622} (dashed curve) and $-U_{4622}$ (solid curves). In the inset, the isovalues of the poloidal component of the magnetic field are plotted for $R_m = 3176$.

U_K, U_F, and U_{4622} by their opposites (or if we replace the pitch angle by its opposite). For U_S, U_K, and U_F, it means that only the leading arms configuration can lead to dynamo action. For U_{4622}, only the configuration with a leading arm surrounded by trailing arms can lead to a dynamo. Increasing the value of $\sigma_\perp/\sigma_\parallel$ does not change this qualitative conclusion (as illustrated in Figure 6 in the Appendix for $U = U_S$).

From Figure 5, we note that the dynamo threshold R_m^c, above which $\gamma > 0$, is much higher for $-U_{4622}$ ($R_m^c = 3176$) than for $-U_S$, $-U_K$, and $-U_F$ ($R_m^c = 106$, 120, and 142). Also, the value of γ is smaller by about 2 orders of magnitude for $-U_{4622}$. This agrees well with (6) as, for NGC 4622, p and Ω' are about 10 times smaller than in the three other cases.

For $-U_S$, $-U_K$, and $-U_F$, there are magnetic mode transitions, from quadrupolar to octopolar at $R_m = 359$, 510, and 680, respectively, and from octopolar to a higher degree at $R_m = 901$, 1295, and 1763, respectively. For $-U_{4622}$, the magnetic eigenmode is quadripolar and generated in the outer part of the conducting domain, corresponding to the leading arms (Figure 5(b)). A 3D representation of the magnetic field lines is shown in the Appendix (Figure 8) for $U = -U_S$ and $U = -U_{4622}$.

3.5. Characteristic Time

In the high R_m limit, and in all four cases $-U_S$, $-U_K$, $-U_F$, and $-U_{4622}$, the growth rate does not decrease toward zero, which is the signature of fast dynamo action (Figure 5). As shown in F. Plunian & T. Alboussière (2022), the dynamo takes place (i) at a characteristic radius where the shear is maximum, located here at $r \sim r_b$, and (ii) with a characteristic time, which is the turnover time at that scale, here $\tau \sim |\Omega(r_b)^{-1}|$. With a characteristic velocity $U \sim 10^2\,\mathrm{km\,s^{-1}}$ (M. Persic et al. 1996) and a characteristic bulge's radius $r_b \sim 1$–$10\,\mathrm{kpc}$, we find that spiral-arm galaxies have a characteristic turnover time $\tau \sim 10^7$–$10^8\,\mathrm{yr}$, which is a fraction of a spiral-arm galaxy's age.

3.6. Characteristic Scale

We note that the larger the Ω, the smaller the vertical magnetic structures (Figure 4), in agreement with the fast dynamo model of F. Plunian & T. Alboussière (2022). The characteristic scale of magnetic structures is of the order of $R_m^{-1/2} r_b$. At this scale, the magnetic diffusion time is equal to the turnover time.

4. Conclusion

In this paper, we studied the question of whether a dynamo effect in a spiral-arm galaxy can be a simple consequence of the existence of its spiral arms. The answer could be yes, provided the arms are leading not trailing, as usually observed in galaxies, or provided the shear increases with r ($|\Omega|' > 0$), which is usually also not observed in galaxies. Having both leading arms and an increasing shear with r would not lead to a dynamo either. Therefore, based on current observations, we do not find any possibility of having a galactic magnetic field generated only by a simple differential rotation, without requiring an effect of turbulence e.g., an alpha effect. This does not mean that the geometry of the arms plays no role. In fact, it remains true that electric currents flow preferentially along the spiral arms of the galaxy, corresponding to an anisotropic electrical conductivity effect. Therefore, a complete model of a galactic dynamo should include at least three effects: differential rotation, the effect of turbulence, like an alpha effect, and an anisotropic effect. We can also think of large-scale fluctuations in azimuthal velocity, so that the sign of Ω' is modified at certain points. It would then be possible for the anisotropic dynamo to take hold. In NGC 4622, the sign of Ω' is indeed changed at $r = 30''$. However, it is accompanied by the transformation of the trailing arms into leading arms, which again rules out the possibility of an anisotropic dynamo. From these observations, we can suggest that the anisotropic dynamo effect induced by shear leads to a selection principle: if condition (7) is applied, then the fast dynamo would produce a strong magnetic field, inducing strong Lorentz forces that would reorganize the differential rotation and/or pitch angle until condition (7) is no longer satisfied. This remains to be demonstrated in more detailed dynamical numerical simulations.

Acknowledgments

We acknowledge the support of the Programme et Équipements Prioritaire pour la Recherche (PEPR Origins) for its financial support. Numerical simulations were carried out using Freefem++ (F. Hecht 2012) and 3D modeling was done using Paraview software (J. Ahrens et al. 2005).

Appendix

In Figure 6(a), the growth rate is plotted versus R_m for $U = -U_S$ and several values of $\sigma_\perp/\sigma_\parallel > 1$. In Figure 6(b), the critical magnetic Reynold number is plotted versus $\sigma_\perp/\sigma_\parallel$.

The magnetic pitch angle, p_B, is defined by

$$p_B = \arctan\left(\frac{B_r}{B_\theta}\right). \tag{A1}$$

In Figure 7(a), the radially averaged magnetic pitch angle $\bar{p}_B$ is plotted versus Rm for $U = -U_K$, $-U_S$, $-U_F$, and $\sigma_\perp/\sigma_\parallel = 10^6$. In the limit of large Rm, $\bar{p}_B$ asymptotically approaches the motion pitch angle p, as already observed in spiral-arm galaxies (C. Van Eck et al. 2015; R. Beck 2016). In Figure 7(b), for $U = -U_S$ and $R_m = 200$, the magnetic pitch angle p_B is plotted versus r for different values of $\sigma_\perp/\sigma_\parallel$.

In Figure 8, a 3D representation of the magnetic field is plotted for (a) $U = -U_S$ and $R_m = 350$, and (b) $U = -U_{4622}$ and $R_m = 3180$.

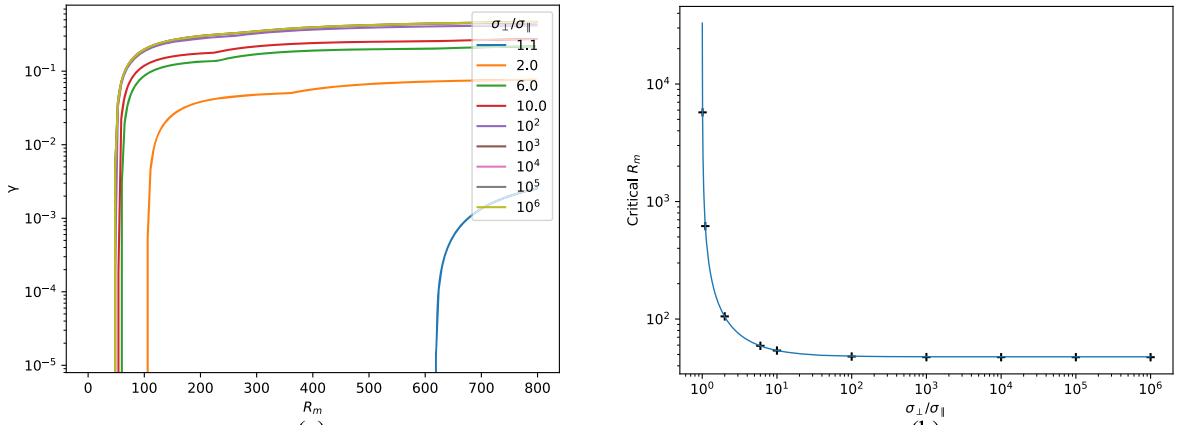

Figure 6. For $U = -U_S$ and different values of $\sigma_\perp/\sigma_\parallel$. (a) The growth rate is plotted vs. R_m. (b) The critical R_m, above which dynamo occurs, is plotted vs. $\sigma_\perp/\sigma_\parallel$.

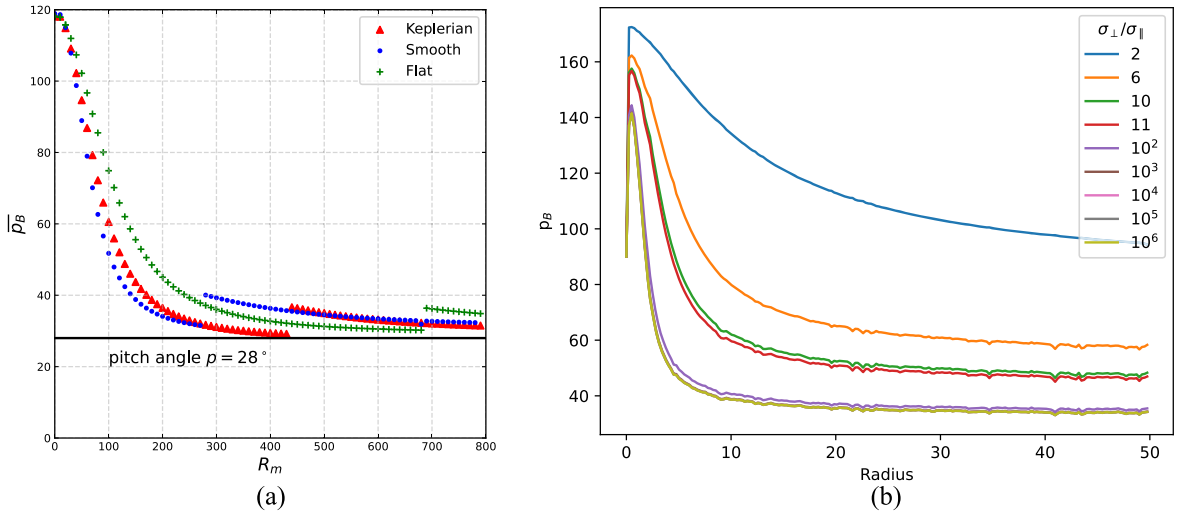

Figure 7. (a) The radial mean of the magnetic pitch angle $\bar{p}_B$ is plotted vs. Rm for $U = -U_K$, $-U_S$, $-U_F$, and $\sigma_\perp/\sigma_\parallel = 10^6$. (b) For $U = -U_S$ and $R_m = 200$, the magnetic pitch angle p_B is plotted vs. r for different values of $\sigma_\perp/\sigma_\parallel$.

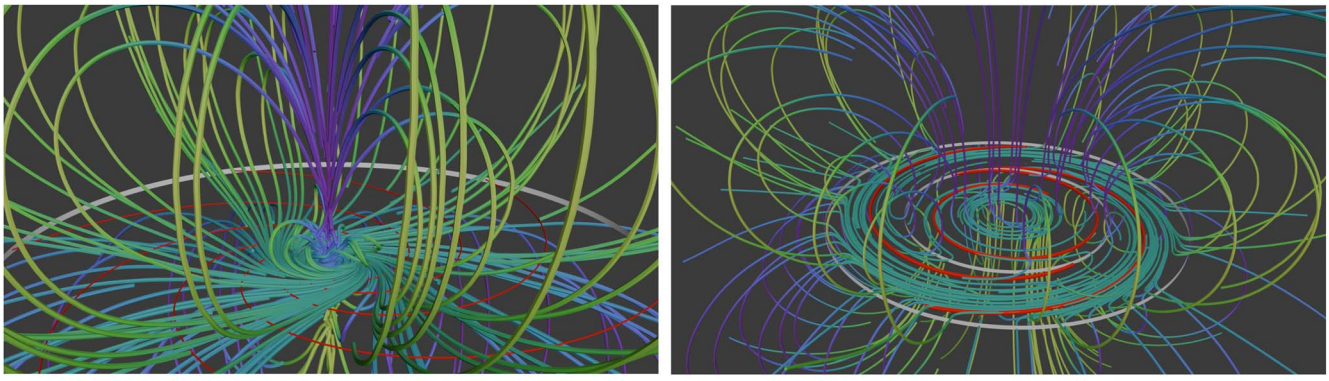

Figure 8. A 3D representation of the magnetic field lines for (a) $U = -U_S$ and $R_m = 350$, and (b) $U = -U_{4622}$ and $R_m = 3180$. The green and blue colors correspond to opposite signs of $\boldsymbol{B}_z$. The red lines are perpendicular to $\boldsymbol{q}$, so in the direction of the spiral arms, assuming axisymmetry. In both panels, the outer gray circular ribbon marks the radial edge of the conducting domain. In the right panel, the inner gray circular ribbons mark the transition between the leading and trailing arms.

References

Ahrens, J., Geveci, B., Law, C., Hansen, C., & Johnson, C. 2005, The Visualization Handbook, 717 (Burlington, MA: Elsevier)
Alboussière, T., Drif, K., & Plunian, F. 2020, PhRvE, 101, 033107
Alboussière, T., Plunian, F., & Moulin, M. 2022, RSPSA, 478, 20220374
Beck, R. 2016, A&ARv, 24, 4
Beck, R., Chamandy, L., Elson, E., & Blackman, E. G. 2019, Galax, 8, 4
Begeman, K. 1987, PhD thesis, Univ. Groningen
Brandenburg, A., & Subramanian, K. 2005, PhR, 417, 1
Buta, R., Crocker, D., & Byrd, G. 1992, AJ, 103, 1526
Buta, R. J., Byrd, G. G., & Freeman, T. 2003, AJ, 125, 634
Byrd, G., & Howard, S. 2019, J. Wash. Acad. Sci., 105, 1
Childress, S., & Gilbert, A. D. 2008, Stretch, Twist, Fold: The Fast Dynamo, 37 (Berlin: Springer)
Davis, B. L., Berrier, J. C., Shields, D. W., et al. 2012, ApJS, 199, 33
Gutiérrez, L., & Beckman, J. E. 2010, ApJL, 710, L44
Hecht, F. 2012, J. Numer. Math., 20, 251
Knapen, J. 1998, MNRAS, 297, 255
Krause, F., & Rädler, K.-H. 1980, Mean-field Mapneto-hydro-dynamics and Dynamo Theory (Berlin: Akademie-Verlag)
Mollá, M., Ferrini, F., & Gozzi, G. 2000, MNRAS, 316, 345
Möllenhoff, C. 2004, A&A, 415, 63
Pasha, I., & Smirnov, M. 1982, Ap&SS, 86, 215
Persic, M., Salucci, P., & Stel, F. 1996, MNRAS, 281, 27
Plunian, F., & Alboussière, T. 2020, PhRvR, 2, 013321
Plunian, F., & Alboussière, T. 2022, JFM, 941, A66
Rincon, F. 2019, JPlPh, 85, 205850401
Rubin, V. C., Ford, W. K., Jr., Thonnard, N., & Burstein, D. 1982, ApJ, 261, 439
Ruderman, M., & Ruzmaikin, A. 1984, GApFD, 28, 77
Savchenko, S., & Reshetnikov, V. 2013, MNRAS, 436, 1074
Schekochihin, A. A., Boldyrev, S. A., & Kulsrud, R. M. 2002, ApJ, 567, 828
Seigar, M., & James, P. 1998, MNRAS, 299, 672
Seigar, M. S., Bullock, J. S., Barth, A. J., & Ho, L. C. 2006, ApJ, 645, 1012
Sofue, Y., & Rubin, V. 2001, ARA&A, 39, 137
Spitzer, L., Jr., & Härm, R. 1953, PhRv, 89, 977
Van Eck, C., Brown, J., Shukurov, A., & Fletcher, A. 2015, ApJ, 799, 35
Zhao, Y.-H., Peng, Q.-H., & Wang, L. 2004, ChJAA, 4, 51